



Developing a Photoacoustic Whole-Breast Imaging System Based on the Synthetic Matrix Array

Guangjie Zhang¹, Wenzhao Li¹, Meng Yang² and Changhui Li^{1*}

¹Department of Biomedical Engineering, College of Engineering, Peking University, Beijing, China, ²Department of Ultrasonography, Peking Union Medical College Hospital, Chinese Academy of Medical Sciences & Peking Union Medical College, Beijing, China

In this study, we reported a photoacoustic (PA) imaging system for whole-breast imaging. Similar to the traditional X-ray mammography, this system slightly compressed the breast by a water tank. The PA signal is acquired via scanning a long unfocused ultrasonic linear array probe over the breast top surface, and the expanded high-energy laser pulses illuminate the breast bottom through a transparent supporting plate. Scanning the unfocused transducer probe is equivalent to a synthetic two-dimensional (2D) matrix array, which significantly increased the field of view (FOV) via a much easier way and at a much lower cost. Our phantom results demonstrated that this system has a great potential for clinical implementation.

OPEN ACCESS

Edited by:

Chao Tian,
University of Science and Technology
of China, China

Reviewed by:

Lei Xi,
Southern University of Science and
Technology, China
Hui Fang,
Shenzhen University, China

*Correspondence:

Changhui Li
chli@pku.edu.cn

Specialty section:

This article was submitted to Medical
Physics and Imaging,
a section of the journal
Frontiers in Physics

Received: 30 August 2020

Accepted: 19 October 2020

Published: 20 November 2020

Citation:

Zhang G, Li W, Yang M and Li C (2020)
Developing a Photoacoustic Whole-
Breast Imaging System Based on the
Synthetic Matrix Array.
Front. Phys. 8:600589.
doi: 10.3389/fphy.2020.600589

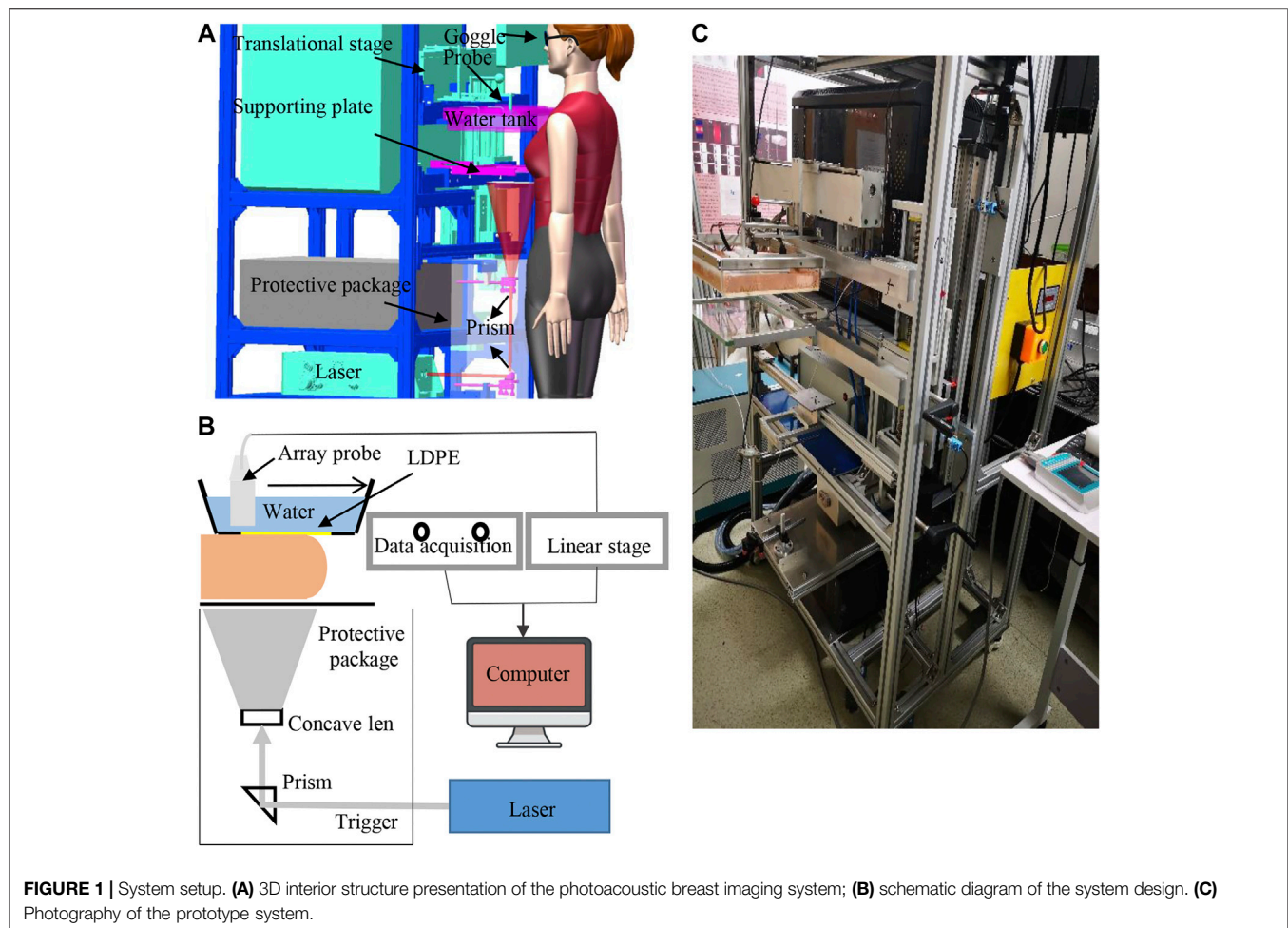
Keywords: photoacoustic imaging, breast imaging, mammography, 3D imaging, synthetic matrix array

INTRODUCTION

Breast cancer is the most common cancer for women and ranks top of newly diagnosed cancers in 2018 [1]. Early detection and accurate diagnosis of breast cancer can substantially improve the survival rate [2–4]. Although X-ray mammography serves as the standard imaging method, it suffers lower sensitivity for dense breasts [5], and the radiation hazard also prevents it to be frequently used. Ultrasound (US) and magnetic resonance imaging (MRI) are also common imaging modalities adjunct to mammography [6–8]. However, MRI not only is expensive and complicated but also often requires exogenous contrast agent. US is the most convenient clinical imaging method, but it primarily depicts the structural information with relatively lower specificity, as well as its diagnosis accuracy highly depends on the physician's personal experience. Over the past decade, the emerging photoacoustic (PA) breast imaging method gained increasing attention with promising clinical study results [9, 10].

Based on the PA effect, PA imaging (PAI) combines the optical contrast and acoustic detection [11]. Via detecting US pressure waves generated through instant thermal expansion after certain tissue (optical absorber) absorbing the energy of the laser pulse, PAI can reconstruct images of those optical absorbers. Because angiogenesis and hypoxia are two typical hallmarks for breast cancer [12, 13] and the hemoglobin in blood is a strong endogenous optical absorber in the near infrared regime, most PA breast imaging systems target the abnormal vasculature, including morphology (such as the vessel density) and function (such as the oxygenation saturation).

Up to now, several PA breast imaging platforms have been developed, which can be classified into two types: local breast imaging based on handheld probes and whole-breast imaging. Owing to its familiarity to physicians, the PA handheld probe has been widely studied [14, 15]. Moreover,



commercial PA/US handheld products are also available [16, 17]. However, handheld probes only image limited part of the breast and suffers artifacts caused by limited-view issue. Therefore, PA whole-breast imaging also gains much attention [9, 18–20]. Most of the PA whole-breast imaging systems require patients to be in a prone position. Toi et al. [14] developed a system with a hemispherical-shaped detector array. Lin et al. [9] scanned the breast with a 220-mm-diameter, 512-element full-ring ultrasonic transducer array, whereas researchers in Twente University used an 80-mm-diameter, 590-element two-dimensional (2D) planar array [21]. Instead of prone position design, Zhixing et al. [19] reported a system similar to the X-ray mammographic geometry in which it employed a 572-element 2D planar array with a diameter of 80 mm lying under the compressed breast. Due to the technical complexity and cost, current 2D planar arrays used in PA breast imaging not only have limited data acquisition channels but also the element size is generally large, which sacrifices the spatial resolution. Compared to the 2D array probe, it is much easier to manufacture a linear array with smaller element size, as well as its parallel data acquisition system. Nikhila et al. [22] presented a dual scan mammoscope system by two focused

array, and they employed the “virtual line” algorithm to successfully improve the elevation resolution. But the inherent focusing characteristic of this probe still limits its effective acquisition angle, making it difficult to image vertically obliquely aligned targets in 3D.

In this work, we presented a prototype PA whole-breast imaging system: photoacoustic synthetic matrix array tomography (PA-Smart). Our design employs the operation posture as in X-ray mammography, where patients stand (or sit) during the imaging procedure. Unlike the work reported in Refs. 19, 22, we scanned the breast with a one-dimensional (1D) unfocused linear probe over the upper surface of the breast. We have previously reported a method to realize a large-scale 2D planar array via scanning an unfocused linear array [23]. Based on this method, our system significantly increased the field of view (FOV) in a much easier way and at a much lower cost for PA breast imaging. At the same time, we used high-energy NIR laser illuminating the bottom of the breast over a large area to deliver enough photons into the breast within the safety limit. The phantom study demonstrated that our system can finish imaging an FOV of more than $10\text{ cm} \times 10\text{ cm} \times 4\text{ cm}$ within 33 s.

METHODS

System Setup

The PA-Smart imaging system is shown in **Figure 1A**. Similar to X-ray mammography, the subject stands in front of the system, and one of the patient's breasts was placed onto a transparent plate (made of glass) and was mildly compressed by the bottom of a water tank above the breast. Slight compression can not only reduce the breast thickness to facilitate light to penetrate but also reduce the tissue movement caused by breathing. An electrical translational stage drives a 1D unfocused linear US array to scan in the water tank at a speed of 3 mm/s. The bottom of the water tank is made by low-density polyethylene (LDPE) material that has a similar acoustic impedance with the breast tissue.

A Q-switched Nd: YAG laser (MQ/X, Beamtech Co., Ltd., China) provided 9-ns 1064-nm laser at a maximum pulse energy of 1.6 J/pulse and a repetition rate of 10 Hz to excite PA signals. The laser beam passed a concave lens and was expanded to be 10 cm in diameter onto the breast's bottom surface, guaranteeing the optical fluence on the tissue surface less than the American National Standards Institute (ANSI) safety limit at 1,064 nm (100 mJ/cm²). To further ensure the safety, laser paths are confined in the protective package, and the only risk comes from the light leaking from the glass. Laser safety goggles are required for both the patient and the physician during examination. Also, the laser system specially designed a visible low-power red guiding light, which shares the same paths with the 1064-nm laser; then, we can double-check the laser alignment before each examination.

Figure 2A demonstrated the mechanism of constructing a synthetic large-scale 2D planar matrix array via scanning a long 1D unfocused array. The array used in this study, as shown in **Figure 2B**, consists of two identical customized unfocused linear array probes (TomoWave Inc., Houston, United States). Each subprobe has 48 elements of 1.0 mm × 1.0 mm, and the pitch is 1.35 mm. The array has a center frequency of 1.2 MHz and the bandwidth covering from 0.5 to 6.0 MHz. The theoretical acceptance angle for each unfocused element is about 45° at 1.5 MHz, guaranteeing to effectively detect PA signals from a large angle, which is essential for 3D reconstruction. The detected PA signal was amplified and recorded by a customized 12-bit data acquisition system (TomoWave Inc., Houston, United States) at a 25 MHz sampling rate.

In the following phantom study, we generally scanned the linear array about 10 cm. Considering the width of each element as 1 mm, scanning 10 cm corresponds to 100 columns of elements ($N = 100$) in **Figure 2A**. The equivalent large-scale 2D planar matrix array has 96×100 (~10 k) elements, leading to a substantially increased field of view (FOV). We employed the universal filtered back projection (FBP) algorithm [24] with a planar detection surface to do the 3D image reconstruction.

Imaging Resolution of the System

The imaging resolution of the system is influenced by several factors, including array's characteristics (element size, pitch, and

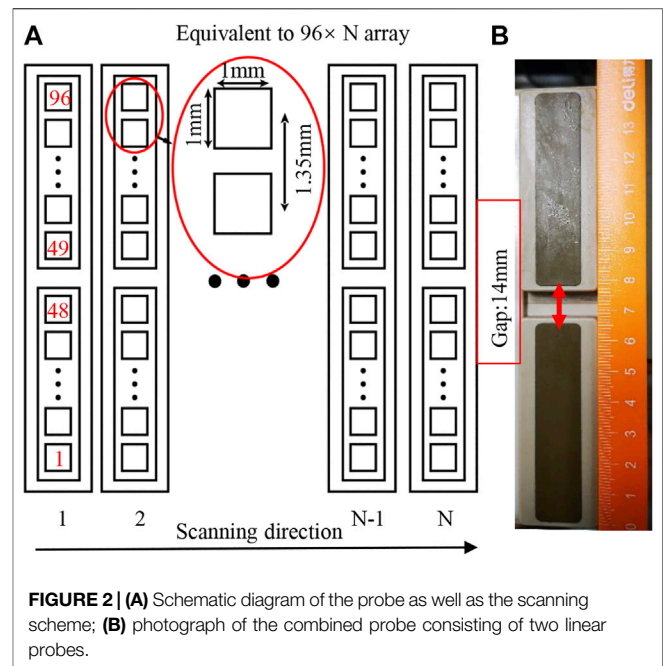


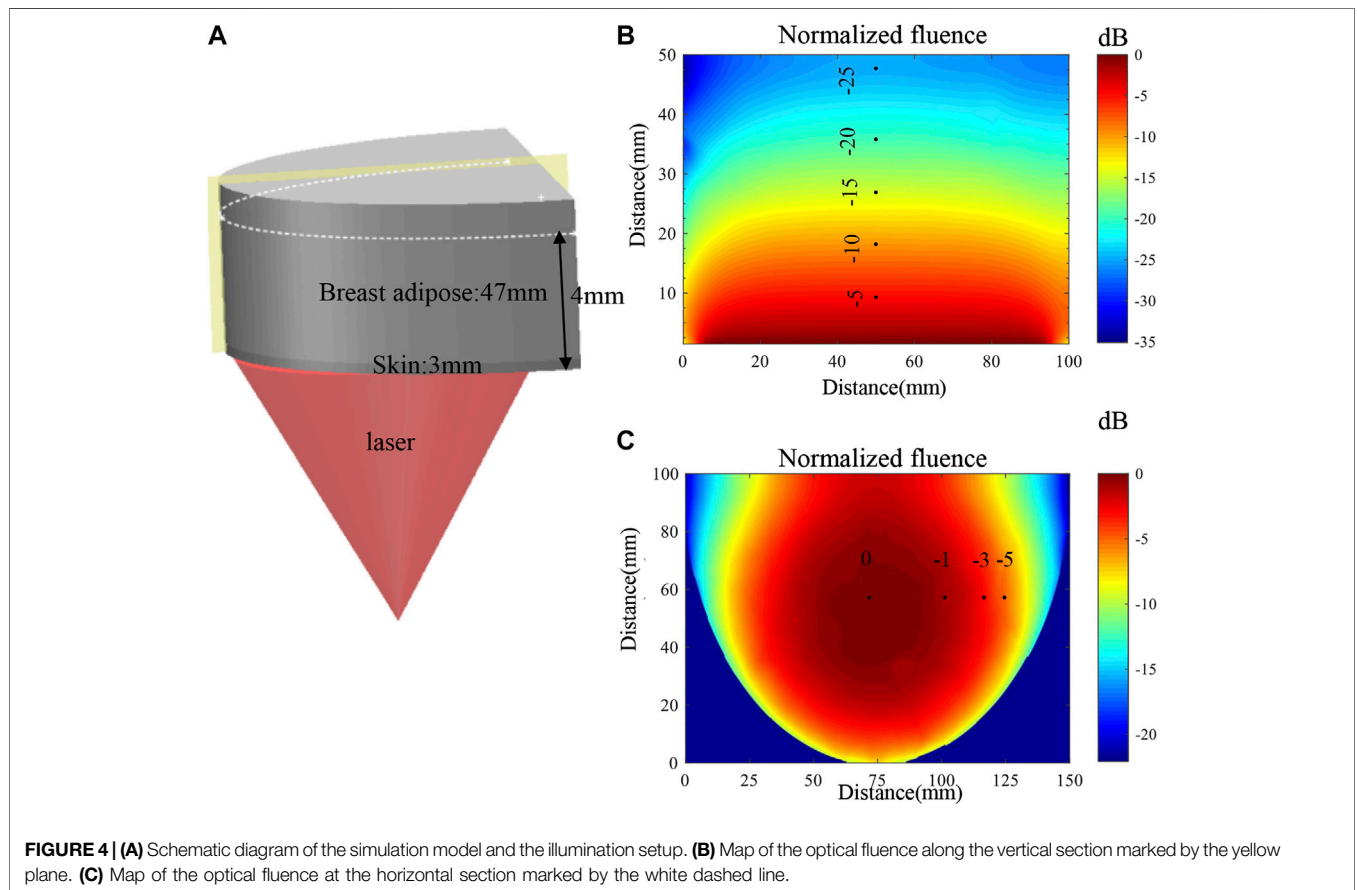
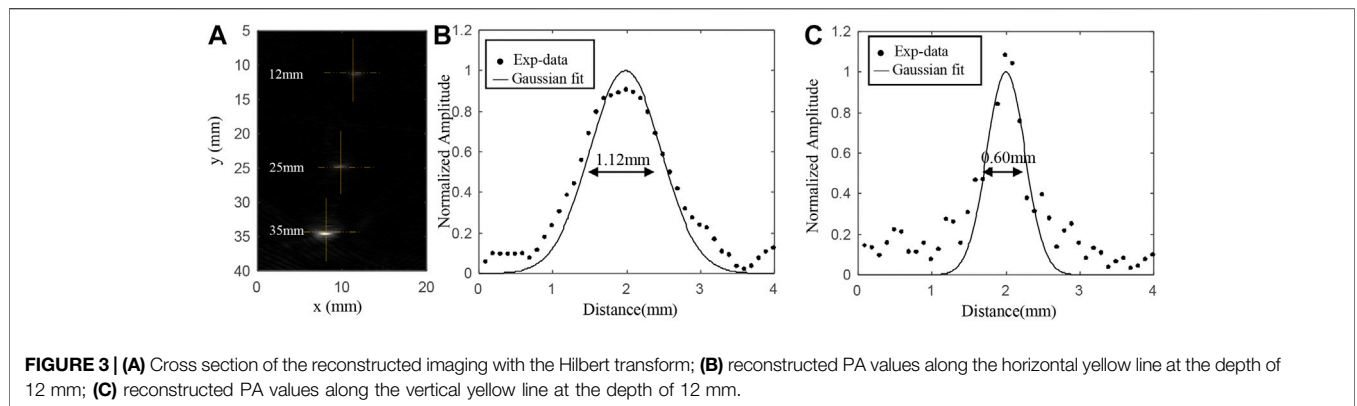
FIGURE 2 | (A) Schematic diagram of the probe as well as the scanning scheme; **(B)** photograph of the combined probe consisting of two linear probes.

bandwidth) and the synthetic numerical aperture. We experimentally measured the spatial resolution by imaging three strands of black human hair buried in a scattering agar phantom, which had a thickness of 5 cm and consisted of 3% agar and 1% intra-lipid.

The three hair strands were horizontally embedded in the agar phantom at depths of 12, 25, and 35 mm from the top surface of the phantom, respectively. **Figure 3A** showed a cross section of the reconstructed image with the Hilbert transform [25]. From these results, we use Gaussian fitting for the values along the three horizontal dashed lines and three vertical solid lines as shown in **Figure 3A**. **Figures 3B and C** presented the fitting results at a depth of 12 mm. According to the results, the lateral resolutions were about 1.12, 1.37, and 1.57 mm at depths of 12, 25, and 35 mm, respectively. And the corresponding elevation resolutions at those three depths are about 0.60, 0.61, and 0.63 mm, respectively.

Simulation Study of the Light Fluence

Considering the significant decrease in light fluence inside the thick breast tissue, we also studied the light fluence distribution inside a breast model by numerical simulation with COMSOL (COMSOL Inc., Sweden). As shown in **Figure 4A**, the breast tissue model is approximated to be a half cylindroid with a thickness of 5 cm. The cylindroid long and short axes are 20 and 15 cm, respectively. The model composes of the skin layer (~3 mm thick) and adipose layer, with the corresponding optical absorption and scattering coefficients being ($\mu_{a1} = 0.1\text{cm}^{-1}$, $\mu'_{s1} = 10\text{cm}^{-1}$) and ($\mu_{a2} = 0.091\text{cm}^{-1}$, $\mu'_{s2} = 6\text{cm}^{-1}$), respectively [26, 27]. The pattern of the expanded laser illuminating onto the bottom of the breast is approximated to be a uniform circle with a 10-cm diameter.



The simulation of the light fluence distribution is based on the diffusion equation for the global region as in Eq. 1, which has been widely employed in PA imaging study [28],

$$-\frac{1}{\mu_{eff}^2} \nabla^2 \phi + \phi = 0, \tag{1}$$

where ϕ is the light fluence rate and μ_{eff} is the effective attenuation coefficient. The calculated normalized optical fluence in the central cut plane (marked as a yellow plane in Figure 4A) is shown in

Figure 4B. Figure 4C presents the calculated normalized optical fluence distributions over a horizontal plane (marked as a white dashed line in Figure 4A, 4 cm from the illuminated bottom surface). The color bar scale of all the fluences is in dB scale. The simulation results implicit that the light fluence could be decreased to two orders less after penetrating 4 cm in the breast, which will definitely influence the reconstructed PA values. Therefore, fluence compensation algorithms are desired, and we will demonstrate it in the phantom study.

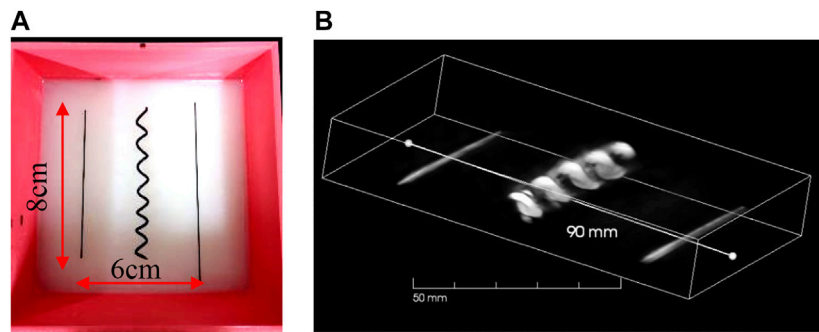


FIGURE 5 | (A) Photograph of carbon rods and helix in scattering medium in phantom study; **(B)** 3D result of carbon rods and helix.

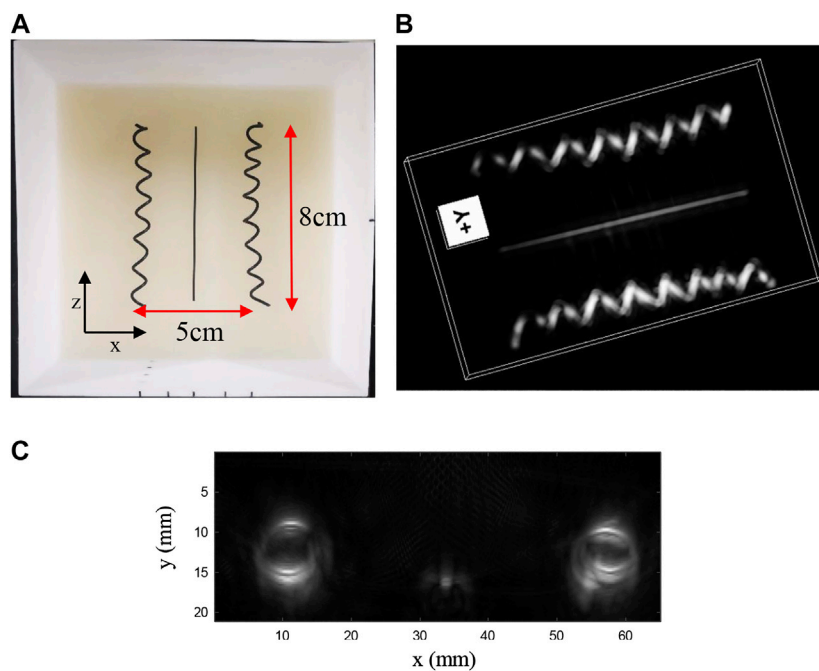


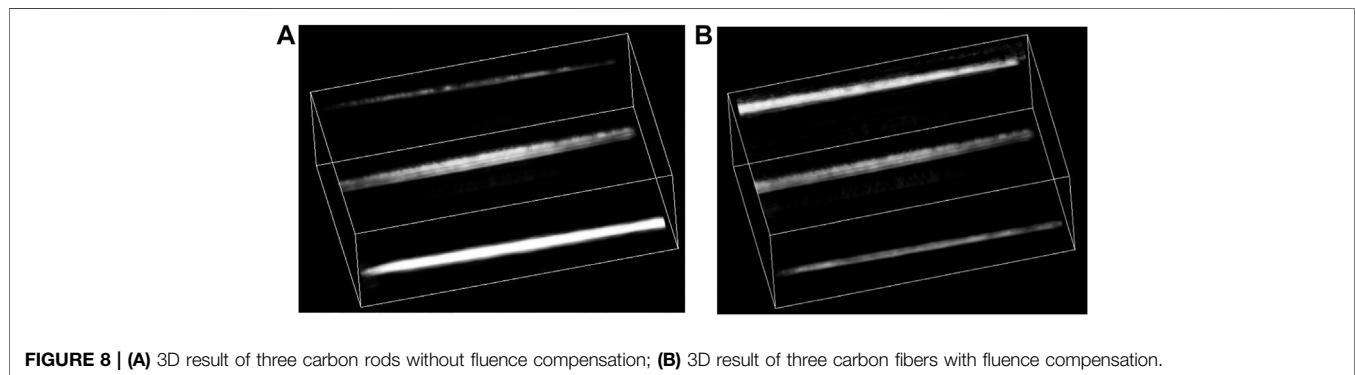
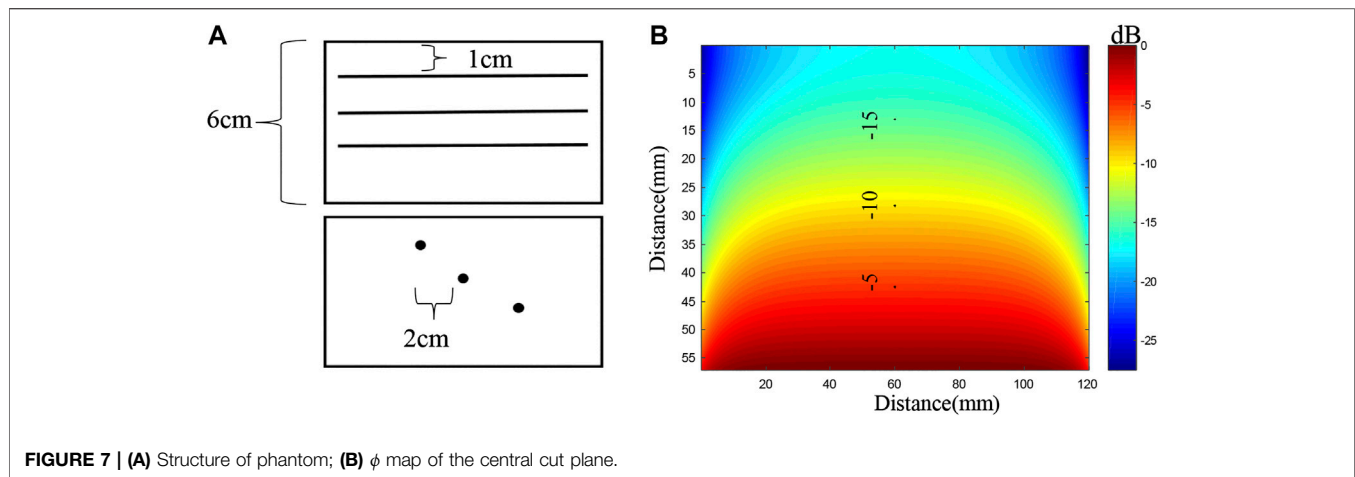
FIGURE 6 | (A) Photograph of carbon rods and helices in scattering medium in phantom study; **(B)** 3D result of carbon rods and helices; **(C)** MAP imaging of one period of the helix.

RESULTS AND DISCUSSION

To validate the system's FOV and the capability of imaging complicated targets, we did two phantom experiments, in which all the imaged targets were buried in the agar phantom made of 3% agar and 1% intra-lipid. In the first phantom, we embedded two carbon rods (0.7 mm in diameter) and one helix object (7 mm in diameter) made from a black strip in a 4-cm-thick agar phantom, as illustrated in **Figure 5A**. These objects were horizontally buried approximately 2.0 cm deep into the phantom, in which the helix was located at the center. The laser illuminated upwardly onto the bottom of the phantom. Then, within 34 s, the array continuously scanned a total length of

100 mm at a speed of 3 mm/s, leading to a large-scale equivalent matrix array of 100 mm \times 130 mm in size and nearly 10k elements (100 \times 96 = 9,600). The 3D reconstructed image is shown in **Figure 5B** with an online animation (movie01). According to the result, not only the two wires but also the helix was well-reconstructed.

To study the potential artifact caused by the limited-view issue, we made the second phantom in which two helix objects (both about 7 mm in diameter) and one carbon fiber (1 mm in diameter) were embedded. Unlike the first phantom, the carbon fiber lied in the center and two helices lied close to the two side edges (also close to the edge of FOV), as shown in **Figure 6A**. The distance from the middle carbon fiber to the



center of the helix is approximately 25 mm. **Figure 6A** was the photograph of the phantom. We scanned a length of total 90 mm, leading to an equivalent large-scale matrix array with 90×106 (~ 9 k) elements. The 3D image reconstruction is shown in **Figure 6B** with an online animation (movie02). Owing to the large FOV and wide acceptance angle, both the helix and carbon fiber were well-reconstructed. In addition, the wide acceptance angle also helps recover oblique surface profile, as shown in **Figure 6C** in which we provide the MAP imaging of one period of the helix, except the middle part where the generated PA wave propagates parallel to the probe, which cannot be detected due to the limited view [29].

Next, to demonstrate the ability of deep imaging, we continued to image three carbon fibers (1 mm in diameter) at 1.0, 2.0, and 3.0 cm depths into the agar phantom, as shown **Figure 7A**. The imaging result is shown in **Figure 8A**. Due to the large difference in the light fluence as shown in **Figure 7B**, the fiber at the deeper location, that is, closer to the illumination source, would have much larger PA value, leading to an apparently thicker diameter in the 3D reconstructed images. Therefore, we applied fluence compensation, and the result is shown in **Figure 8B**.

CONCLUSION

In this work, we developed a PA-Smart whole-breast imaging system. The proposed imaging posture is familiar to physicians and facilitates patients' examination. The large FOV of the system is achieved based on the synthetic matrix array method via scanning an unfocused linear array. Besides, the synthetic 2D array can have less reconstruction artifacts, which is crucial for whole-breast imaging. We did phantom experiments to validate the performance of the system. The clinical study is our next step to explore the power of this system.

However, there is relatively lower reconstruction quality of the side of the helix, which is caused by the "limited view" issue. In addition, the current resolution is about 1 mm, which is not suitable for imaging fine vasculature in breast tumor. Moreover, the 14-mm physical gap between two independent linear probes also degraded the imaging quality, especially for those just under the gap. We are working on a new probe with longer length and more elements with smaller element size. New reconstruction algorithms and machine learning will be applied to help solving problems with the limited view.

DATA AVAILABILITY STATEMENT

The original contributions presented in the study are included in the article/supplementary material, further inquiries can be directed to the corresponding author.

AUTHOR CONTRIBUTIONS

CL conceived the idea. GZ designed the system and did data analysis. All the authors contributed to the discussion on the results for this manuscript.

REFERENCES

- Siegel RL, Miller KD, Jemal A. Cancer statistics, 2018. *Cancer J Clinicians* (2018) 68(1):7–30. doi:10.3322/caac.21442.
- Elmore JG, Armstrong K, Lehman CD, Fletcher SW. Screening for breast cancer. *J Am Med Assoc* (2005) 293(10):1245–56. doi:10.1001/jama.293.10.1245.
- Bray F, McCarron P, Parkin DM. The changing global patterns of female breast cancer incidence and mortality. *Breast Canc Res* (2004) 6(6):229. doi:10.1186/bcr932.
- Miller AB, Wall C, Baines CJ, Sun P, To T, Narod SA. Twenty five year follow-up for breast cancer incidence and mortality of the Canadian National Breast Screening Study: randomised screening trial. *Bmj* (2014) 348:g366. doi:10.1136/bmj.g366.
- Freer PE. Mammographic breast density: impact on breast cancer risk and implications for screening. *Radiographics* (2015) 35(2):302–15. doi:10.1148/rg.352140106.
- Madjar H. Role of breast ultrasound for the detection and differentiation of breast lesions. *Breast Care* (2010) 5(2):109–14. doi:10.1159/000297775.
- Taylor KJW, Merritt C, Piccoli C, Schmidt R, Rouse G, Fornage B, et al. Ultrasound as a complement to mammography and breast examination to characterize breast masses. *Ultrasound Med Biol* (2002) 28(1):19–26. doi:10.1016/s0301-5629(01)00491-4.
- Saslow D, Boetes C, Burke W, Harms S, Leach MO, Lehman CD, et al. American Cancer Society guidelines for breast screening with MRI as an adjunct to mammography. *Cancer J Clin* (2007) 57(2):75–89. doi:10.3322/canjclin.57.2.75.
- Lin L, Hu P, Shi J, Appleton CM, Maslov K, Li L, et al. Single-breath-hold photoacoustic computed tomography of the breast. *Nat Commun* (2018) 9(1):2352. doi:10.1038/s41467-018-04576-z.
- Becker A, Masthoff M, Claussen J, Ford SJ, Roll W, Burg M, et al. Multispectral optoacoustic tomography of the human breast: characterisations of healthy tissue and malignant lesions using a hybrid ultrasound-optoacoustic approach. *Eur Radiol* (2017) 28(2):602–609. doi:10.1007/s00330-017-5002-x.
- Wang LV, Hu S. Photoacoustic tomography: *in vivo* imaging from organelles to organs. *Science* (2012) 335(6075):1458–62. doi:10.1126/science.1216210.
- Folkman J. Angiogenesis in cancer, vascular, rheumatoid and other disease. *Nat Med* (1995) 1(1):27–30. doi:10.1038/nm0195-27.
- Carmeliet P, Jain RK. Angiogenesis in cancer and other diseases. *Nature* (2000) 407:249. doi:10.1038/35025220.
- Neuschler EI, Butler R, Young CA, Barke LD, Bertrand ML, Bohm-Velez M, et al. A pivotal study of optoacoustic imaging to diagnose benign and malignant breast masses: a new evaluation tool for radiologists. *Radiology* (2018) 287(2):398–412.
- Diot G, Metz S, Noske A, Liapis E, Schroeder B, Ovsepian SV, et al. Multispectral optoacoustic tomography (MSOT) of human breast cancer. *Clin Cancer Res* (2017) 23(22):6912–22.
- Zhou Y, Tripathi SV, Rosman I, Ma J, Hai P, Linette GP, et al. Noninvasive determination of melanoma depth using a handheld photoacoustic probe. *J Invest Dermatol* (2017) 137(6):1370–2. doi:10.1016/j.jid.2017.01.016.
- Neuschmelting V, Burton NC, Lockau H, Urich A, Harmsen S, Ntziachristos V, et al. Performance of a multispectral optoacoustic tomography (MSOT) system equipped with 2D vs. 3D handheld probes for potential clinical translation. *Photoacoustics* (2016) 4(1):1–10. doi:10.1016/j.pacs.2015.12.001.
- Toi M, Asao Y, Matsumoto Y, Sekiguchi H, Yoshikawa A, Takada M, et al. Visualization of tumor-related blood vessels in human breast by photoacoustic imaging system with a hemispherical detector array. *Sci Rep* (2017) 7:41970. doi:10.1038/srep41970.
- Xie Z, Hooi FM, Fowlkes JB, Pinsky RW, Wang X, Carson PL. Combined photoacoustic and acoustic imaging of human breast specimens in the mammographic geometry. *Ultrasound Med Biol* (2013) 39(11):2176–84. doi:10.1016/j.ultrasmedbio.2013.05.018.
- Asao Y, Hashizume Y, Suita T, Nagae K-i, Fukutani K, Sudo Y, et al. Photoacoustic mammography capable of simultaneously acquiring photoacoustic and ultrasound images. *J Biomedical Optics* (2016) 21(11):116009. doi:10.1117/1.jbo.21.11.116009.
- Heijblom M, Piras D, Xia W, van Hespden JCG, Klaase JM, van den Engh FM, et al. Visualizing breast cancer using the Twente photoacoustic mammoscope: what do we learn from twelve new patient measurements? *Opt. Express* (2012) 20(11):11582–97. doi:10.1364/oe.20.011582.
- Nyayapathi N, Takabe K, Xia J, Lim R, Zhang H, Zheng W, et al. Dual scan mammoscope (DSM) - a new portable photoacoustic breast imaging system with scanning in craniocaudal plane. *IEEE Trans Biomed Eng* (2019) 67(5):1321–1327. doi:10.1109/tbme.2019.2936088.
- Tan Y, Xia K, Ren Q, Li C. Three-dimensional photoacoustic imaging via scanning a one dimensional linear unfocused ultrasound array. *Opt Express* (2017) 25(7):8022–8.
- Xu M, Wang LV. *Universal back-projection algorithm for photoacoustic computed tomography* (2007) 1539–3755.
- Li G, Li L, Zhu L, Xia J, Wang LV. Multiview Hilbert transformation for full-view photoacoustic computed tomography using a linear array. *J Biomed Opt* (2015) 20(6):066010. doi:10.1117/1.jbo.20.6.066010.
- Cheong WF, Prael SA, Welch AJ. A review of the optical properties of biological tissues. *IEEE J Quantum Electron* (1990) 26(12):2166–85. doi:10.1109/3.64354.
- Sandell JL, Zhu TC. A review of *in-vivo* optical properties of human tissues and its impact on PDT. *J Biophot* (2011) 4(11-12):773–87. doi:10.1002/jbio.201100062.
- Wang LV, Wu HI. *Biomedical optics: principles and imaging*. John Wiley & Sons (2012).
- Xu Y, Wang LV, Ambartsoumian G, Kuchment P. Reconstructions in limited-view thermoacoustic tomography. *Med Phys* (2004) 31(4):724–33. doi:10.1118/1.1644531.

Conflict of Interest: The authors declare that the research was conducted in the absence of any commercial or financial relationships that could be construed as a potential conflict of interest.

Copyright © 2020 Zhang, Li, Yang and Li. This is an open-access article distributed under the terms of the Creative Commons Attribution License (CC BY). The use, distribution or reproduction in other forums is permitted, provided the original author(s) and the copyright owner(s) are credited and that the original publication in this journal is cited, in accordance with accepted academic practice. No use, distribution or reproduction is permitted which does not comply with these terms.